

Cancer Immunotherapy Based on Carbon-Quantum-Dots

Tao Liang

University of Macau

Josh Haipeng Lei

University of Macau

Jinsong Tao

University of Macau

Sen Guo

University of Macau <https://orcid.org/0000-0002-2681-0576>

Hanlu Gao

University of Macau

Lipeng Zhu

University of Macau

Yinning Zhou

University of Macau

Youcheng Liu

University of Macau

Long Xi

University of Macau

Haibo Tong

University of Macau

Enshan Liu

University of Macau

Bohan Zhang

University of Macau

Heng Sun

University of Macau

Huiqi Zhang

University of Macau

Kathy Qian Luo

University of Macau

Qi Zhao

University of Macau

Tzu-Ming Liu

University of Macau

Defang Ouyang

University of Macau

Wei Ge

University of Macau

Ying Zheng

University of Macau

Chuxia Deng

University of Macau

Zikang Tang (✉ zikang@um.edu.mo)

University of Macau <https://orcid.org/0000-0001-9998-4940>

Songnan Qu

University of Macau

Research Article

Keywords: Carbon Quantum Dots, Cancer Immunotherapy

Posted Date: April 28th, 2021

DOI: <https://doi.org/10.21203/rs.3.rs-457550/v2>

License:   This work is licensed under a Creative Commons Attribution 4.0 International License.

[Read Full License](#)

Cancer Immunotherapy Based on Carbon-Quantum-Dots

Tao Liang^{# 1}, Josh Haipeng Lei^{# 3}, Jinsong Tao^{# 4}, Sen Guo³, Hanlu Gao⁴, Lipeng Zhu³,
Yinning Zhou^{1,2}, You-Cheng Liu³, Long Xi⁴, Haibo Tong³, Enshan Liu¹, Bohan Zhang¹,
Heng Sun³, Huiqi Zhang¹, Kathy Qian Luo^{2,3}, Qi Zhao^{2,3}, Tzu-Ming Liu^{2,3}, Defang
Ouyang⁴, Wei Ge³, Ying Zheng^{4*}, Chu-Xia Deng^{2,3*}, Zikang Tang^{1,2*}, Songnan Qu^{1,2*}

¹ Institute of Applied Physics and Materials Engineering, University of Macau, Macau SAR, China

² MOE Frontier Science Centre for Precision Oncology, University of Macau, Macau SAR, China

³ Faculty of Health Sciences, University of Macau, Macau SAR, China

⁴ State Key Laboratory of Quality Research in Chinese Medicine and Institute of Chinese Medical Sciences, University of Macau, Macau SAR, China

* Corresponding authors, emails: songnanqu@um.edu.mo; zktang@um.edu.mo; cxdeng@um.edu.mo; yzheng@um.edu.mo

These authors contributed equally to this work.

Abstract

Cancer immunotherapy based on carbon-quantum-dots (CQDs) has proven effective. The CQDs composited cancer cell (CM-cancer) exhibit robust customized immunogenicity, which can recruit macrophages and dendritic cells to effectively deliver the cancer antigens into lymph nodes to activate CD8⁺ T cells, and eventually leads to an anti-cancer immune response all over the body. The CM-cancer is not only able to inhibit primary tumors, but also clearly eliminate metastatic tumors. Our research demonstrates a promising personalized cancer immunotherapeutic technology for potential clinical applications.

30 Cancer is one of the leading causes of death in the world. It is the central research topic
31 on cancer immunotherapy via training the immune system to recognize cancer-specific
32 antigens (neoantigens) following up to kill the cancer cells and overcome cancer
33 recurrence and metastasis. Cancer cells exhibit highly distinct compositions of mutation
34 with limited overlapping similarities among patients^{1,2}. Personalized cancer vaccines
35 are vigorously developed vaccine strategies that aim to modulate the innate and
36 adaptive immune systems for activating anticancer immunity with neoantigens³⁻⁵.
37 Although recent progresses in massive parallel sequencing as well as machine learning
38 make cancer vaccine more feasible, efficient screening and identifying neoantigens for
39 patients is still challenging. A full course of the identification process is high cost and
40 time consuming.^{6,7} Furthermore, cancer vaccines that target multiple neoantigens are
41 considered more effective than targeting a single neoantigen⁸⁻⁹. However, it is
42 extremely challenging to design and produce personalized multi-targeted cancer
43 vaccines within a reasonable short preparation time at affordable cost to serve ordinary
44 cancer patients. Herein, we reported a novel route of cancer immunotherapy based on
45 CQDs. The CM-cancer can recruit macrophages (MPs) as well as dendritic cells (DCs)
46 to effectively deliver the cancer antigens into lymph nodes and eventually leads to
47 specific anti-cancer immune response for the whole body. The CM-cancer is not only
48 able to inhibit primary tumors, but also clearly eliminate metastatic tumors. In this
49 process, the extremely troublesome and time-consuming neoantigen identification are
50 smartly avoided and passed it to antigen presentation cells (APCs) like MPs or DCs,
51 which are of distinct and incomparable advantages for customized cancer
52 immunotherapy.

53 Cancer cells are a natural source for multiple cancer neoantigens, including those
54 not yet identified¹⁰. However, a whole-cancer-cell vaccination always lacks robust
55 immune stimulation, and limited anti-cancer responses¹¹. The primary reasons for this
56 may attributed to most contained proteins in cancer cells being self-body proteins,
57 which have very low immunogenicity, and express weak “eat me” signal to APCs.
58 Derived from normal cells variations, the cancer cells contain multiple immune

59 inhibitory proteins, such as CD24, CD31, CD47, which express “don’t eat me” signal
60 to prevent self-body phagocytosis^{12–15}. All these lead to low cellular uptake efficiency
61 of the neoantigens by APCs, and their inefficient accumulation in lymphatic nodes
62 result in the non-effective anti-cancer T-cell activation. In recent advances, many
63 strategies were proposed to enhance the immunogenicity of the cancer cells by coupling
64 with adjuvant or blocking the immune inhibitory proteins on cancer cells^{16–19}. However,
65 these methods cannot inherently change or enhance the immunogenicity of the cancer
66 cells in large extent. To achieve satisfied anti-cancer immunotherapy, immune
67 checkpoint blockade (ICB) reagents are then commonly adopted in combination^{20–22}.

68 CQDs are promising biomedical materials due to their excellent biocompatibility
69 and non-toxicity^{23–25}. Herein, we develop a facile CQD-based technology to enhance
70 the immunogenicity of cancer cells by composing with CQDs for personalized cancer
71 immunotherapy. In vitro, the CM-cancer hyperactivate MPs with enhanced cellular
72 uptake efficiency and increased MHC-II expression. In vivo, the CM-cancer robustly
73 triggers immune response to recruit MPs and DCs, then engulf and deliver the cancer
74 antigens into the lymph nodes to activate CD8⁺ T cells, eliciting a powerful whole body
75 anti-cancer immune response. Furthermore, we also demonstrate that vaccination with
76 CM-4T1 not only inhibit the primary tumors and prevent from metastasis, but also
77 eliminate the metastatic tumors in the post-surgical 4T1 cancer model with excellent
78 prognosis.

79

80 **Results**

81 To awaken the immune system precisely functioning to cancers, a potential
82 solution is to change the conformational structures of the self-body proteins on the
83 cancer cell surface to enhance the “eat me” signal and weaken the “don’t eat me” signal
84 simultaneously.^{12–15} Unfortunately, researchers have suffered from laboursome and
85 troublesome procedures based on current precise protein modification strategies to
86 achieve these goals. Instead, we developed a facile CQD-based technology.

87 The CQDs were synthesized according to literature²⁶ As shown in the

88 transmission electron microscope (TEM) image (Fig. 1a), the diameters of the CQDs
89 range from 2 nm to 5 nm with clear 0.21 nm lattice fringes, which corresponds to (100)
90 plane of graphite. The heights of the CQDs range from 2 nm to 5 nm as shown in the
91 atomic force microscope (AFM) image (Fig. 1b). The elemental compositions of the
92 CQDs are revealed by energy-dispersive X-ray spectroscopy (EDS) profiles, which
93 demonstrates the presence of C, O, N, and S elements.

94 For applications in biomedical and clinical fields, the cytotoxicity of the CQDs
95 was examined in several cell systems. The CQDs did not affect cell viability even with
96 concentrations up to 500 µg/ml, indicating non- or extremely low cytotoxicity. MPs and
97 DCs are potent antigen-presenting cells and they play Crucial roles in the cancer
98 immunotherapy²⁹.

99 We adopted RAW264.7 (a murine MP cell line), *in vitro*, to analyze the behaviors
100 of MPs affected, by inactivated cancer cells, CQDs and CM-cancer cells, respectively.
101 As shown in Fig. 2a, after 6 hr co-cultivation with CM-4T1, the RAW264.7 cells not
102 only increased in cell size but also were hyperactivated into dendritic-like morphology³².
103 While no obvious morphological or size changes were observed the RAW264.7 cells
104 cultivated only with phosphate buffered saline (PBS), CQDs, and heat-shocked 4T1
105 cells (H-4T1) with DID700 dye labeled (DID700 dye molecules emit fluorescence in
106 650-750 nm), respectively. According to the CLSM images, the hyperactivated
107 RAW264.7 cells contained some red emissive objects which were from the endocytosed
108 CM-4T1 and their degradation products, while nearly no red fluorescent species were
109 observed in the RAW264.7 cells co-cultivated with CQDs or DID700-labeled H-4T1.
110 Obviously, the CM-4T1 co-cultivated RAW264.7 cells exhibited much stronger
111 phagocytic activity than the inactivated pure H-4T1. Furthermore, flow cytometric
112 analysis detected much greater up-regulation of MHC Class II expression on the CM-
113 4T1 co-cultivated RAW264.7 cells than that co-cultivated with CQDs or H-4T1 cells
114 (Fig. 2b), indicating stronger antigen-presenting ability of the CM-4T1 hyperactivated
115 RAW264.7 cells.

116 To visualize the hyperactivated behavior of MPs triggered by the CM-cancer *in*

117 *vivo*^{33,34}, a *Tg (mpeg1:EGFP)* transgenic zebrafish model whose MPs specifically
118 expressed green fluorescence protein (EGFP)^{35,36} was examined by abdominal
119 injection into the therapy group of (Z0) CQD-modified melanoma B16F10 cells (CM-
120 B16F10), and control groups of (Z1) PBS, (Z2) CQDs, and (Z3) heatshocked B16F10
121 cells (H-B16F10) with DiI dye labeled (DiI dye molecules emit fluorescence in 555-
122 650 nm), respectively. At the 6th hr. after injection, no significant recruitment of MPs
123 (green) were observed from the control groups of (Z1)-(Z3) (Fig. 2c). In obvious
124 contrast, the zebrafish with abdominal injection of the CM-B16F10 demonstrated a
125 significant recruitment of MPs, which were well overlapped within the area of red
126 fluorescent signals coming from the injected CM-B16F10 (Fig. 2c). These phenomena
127 indicated that the MPs were successfully recruited to engulf the injected CM-B16F10.
128 At the 24th hr after CM-B16F10 injection, the number of the recruited MPs was
129 significantly decreased, while merged yellow signals overlapped from the MPs (green)
130 and the engulfed CM-B16F10 (red) were observed to drain into the abdominal
131 subcutaneous lymph (Fig. 2c)³⁷. To visualize the anti-cancer response triggered by the
132 CM-cancer vaccine in vivo, the DiI (red fluorescence) labelled B16F10 cancer
133 xenografts were constructed in *Tg (mpeg1:EGFP)* and *Tg (lck:EGFP)* transgenic
134 zebrafish models, respectively, whose MPs and T cells express green fluorescence³⁸.
135 The CM-B16F10 (~40 cells, 4 nl) were intraperitoneally injected into the 3-day cancer
136 xenograft transgenic zebrafishes. The anti-cancer MPs and T cells response after the
137 CM-B16F10 vaccine injections were observed by CLSM. As shown in Fig. 2d, a
138 number of MPs were firstly recruited to the cancer site and then infiltrated into the
139 cancer after the CM-B16F10 treatment. The activated T cells were then followup
140 recruited to the cancer site, infiltrated into the cancer with merged yellow dots (Fig. 2e).
141 Actions of the T cells attacking the cancer cells were clearly seen in the image, as
142 evidenced by gradual decrease of the cancer sizes in three days after the CM-B16F10
143 vaccine injection. In contrast, no significant activated T cells were found in the control
144 group.

145 The CM-cancer induced anti-cancer effect was further evaluated in a B16F10-C3

146 cancer xenograft zebrafish model. The B16F10-C3 cell line was generated by
147 transfecting the plasmid DNA of a CFP (donor)/YFP (acceptor) FRET-based
148 (Fluorescence Resonance Energy Transfer) sensor caspase-3 (C3) into the B16F10 cells,
149 which could serve as a monitor of the cancer cell proliferation growth by YFP imaging
150 (green fluorescence) and detect the caspase-3 activation dependent apoptosis by FRET
151 imaging (blue fluorescence)^{39,40}. The vaccinated therapy group of (B0) CM-B16F10-
152 C3 (~40 cells, 4 nl), and the control groups of (B1) PBS (4 nl), (B2) pure CQDs (4 nl,
153 200 µg/ml), and (B3) heat-shocked B16F10-C3 (H-B16F10-C3) (~40 cells, 4 nl) were
154 intraperitoneally injected into the 3-day B16F10-C3 cancer xenograft A/B wild type
155 zebrafishes, respectively. The cancer growth was monitored by the YFP imaging at
156 predetermined times. The therapy group (B0) showed very significant inhibition of the
157 cancer, in a sharp contrast with those in the control groups of (B1)-(B3). More
158 excitingly, after the CM-B16F10 vaccination, the cancer nearly disappeared on the day
159 6 and totally disappeared on the day 8, while the cancer growths of the three control
160 groups were uncontrolled, and eventually all zebrafishes died starting from the days 7
161 to 8 after the cancer plantation. The apoptosis of the xenograft cancer cells in zebrafish
162 was monitored by FRET imaging which has a living indicator by YFP (acceptor) signal
163 (green), and apoptosis indicator by CFP (donor) signal (blue). We observed that the
164 living cancer cells (green) were proliferating rapidly in the control groups of (B1)-(B3)
165 from the 3rd day to the 6th day and no apoptosis of cancer cells occurred. In contrast,
166 the apoptosis of cancer cells (blue) in the therapy group of (B0) was very obvious in
167 single cell level on the 6th day, which lively visualized the anti-cancer effect triggered
168 by the CM-cancer vaccination.

169 The transportation of the CM-cancer vaccination to lymph nodes with activation
170 of MPs and DCs, and anti-cancer response were further investigated in a mouse model.
171 The therapy group of (L0) CM-4T1 (CQDs: 200 µg/ml, cells: 1×10^7 /ml, 100 µl), and
172 the control groups of (L1) PBS (pH 7.4, 100 µl), (L2) pure CQDs (CQDs: 200 µg/ml,
173 100 µl), and (L3) DID700 dye labeled H-4T1 (cells: 1×10^7 /ml, 100 µl) were
174 intraperitoneal injected into the four groups of Balb/c mice, respectively. The mice were

175 sacrificed at different time points (ranging from 4 hr to 24 hr) after the injections, whose
176 inguinal lymph nodes were collected for histological analysis (Fig. 3). In the therapy
177 group (L0), intensive near infrared (NIR) fluorescence signal (from the combined
178 CQDs) was observed just after 4 hr of vaccination, and then the signal was gradually
179 weakened but retained in the lymph node till to 24 hr. In the control group of (L3), no
180 any labeled-dye fluorescence (NIR) was observed in the lymph node within 24hr after
181 injection, implying that the pure H-4T1 could hardly be delivered to the lymph nodes
182 for activating immune system. Predictably, the other two control groups of (L1) and
183 (L2) did not lead any immune response. The experimental fact indicated that the CM-
184 4T1 vaccine could effectively be drained to lymph nodes. To further evaluate the
185 immune response of the CM-cancer in lymph nodes, 4 μm -thick inguinal lymph nodes
186 tissue sections from the four groups after injection at 4 hr and 24 hr were stained with
187 anti-CD8⁺ (brown), IFN- γ (brown), F4/80 (brown) and CD11c (brown), respectively.
188 At 4 hr after the injection, CD11c, F4/80, IFN- γ , and CD8⁺ expression were obviously
189 increased in the therapy group (L0), indicating activated MPs and DCs could drain to
190 the lymph nodes and effectively activated cytotoxic T cells at about 4 hr after the CM-
191 4T1. At 24 hr after injection, the CD11c, F4/80, IFN- γ , and CD8⁺ still retained high
192 expression in the therapy group (L0). During the studying period, only slightly
193 increased expressions of CD11c, F4/80 and CD8⁺ were observed in the L3 groups at 24
194 hr after H-4T1. All these results demonstrated that vaccination with CM-cancer could
195 effectively recruit and hyperactivate MPs and DCs. By engulfing the CM-cancer, the
196 delivery of cancer antigens were greatly enhanced to lymph nodes and triggered robust
197 cytotoxic T cells response, which was in an obvious contrast with the heat-shocked
198 pure cancer cells vaccination. Noted that for the pure CQDs group, we also observed
199 the delivering of CQDs to lymph nodes, as evidenced by the NIR fluorescence from
200 CQDs which reached to the maximum intensity at around 2 hr. After that, the NIR
201 fluorescence gradually lost its intensity, and eventually vanished at 24 hr, implying the
202 totally clearance of CQDs out of body. Different from the CM-4T1, however, the pure
203 CQDs did not trigger anti-cancer immune response.

204 To further study the immune response and immunotherapy effect of the CM-
205 cancer, protocols of CM-cancer were designed on two murine tumor models, which
206 were 545 cells (Brca1-deficiency tumor cells) in FVB mice and 4T1 in Balb/c mice, as
207 shown in Fig. 4a. Allograft tumors were established by implanting 545 cells (5×10^5
208 cells) and 4T1 cells (5×10^5 cells) into the 4th mammary fad pads of a normal female
209 FVB and Balb/c mice, respectively. We studied the effect on the therapy group of (P0)
210 with intraperitoneal injection of the CM-545 and CM-4T1 (CQDs: 200 $\mu\text{g/ml}$, cells:
211 $1 \times 10^7/\text{ml}$, 200 μl) in the corresponding murine tumor model in comparison with those
212 control groups by injecting: (P1) PBS (pH 7.4, 200 μl), (P2) pure CQDs (200 $\mu\text{g/ml}$,
213 200 μl), (P3) H-545 or H-4T1 (cells: $1 \times 10^7/\text{ml}$, 200 μl), and (P4) CM-EMT6 (CQDs:
214 200 $\mu\text{g/ml}$, cells: $1 \times 10^7/\text{ml}$, 200 μl), respectively. We specially designed the control
215 group (P4) for the sake of testing cross-therapy effect on the 545 and 4T1 carcinoma
216 using the CM-EMT6. As presented in Fig. 4b, the 545 tumor growth of the CM-545
217 therapy group (P0) was significantly inhibited ($p < 0.0001$) in comparison with the
218 control groups (P1-P3) and the Cross-therapy group (P4) as well. It should be noted that
219 the 545 tumor was not effectively inhibited in the cross-therapy group (P4), implying
220 an important fact that the anti-tumor response could only be specifically triggered by
221 the CM-cancer fabricated with the exact same kind of cancer cells. All of the mice in
222 P0 group were tumor-free or without detectable tumor foci after the CM-545
223 treatment on the day 40 and no mice died in three months (Fig. 4c). Similar anti-tumor
224 response could also be observed in the therapy group with CM-4T1 in Balb/c mice with
225 4T1 tumor, as shown in Fig. 4d. We further conducted flow cytometric analyses using
226 various markers. The data revealed a significant increase of the percentage of activated
227 CD8^+ T cells in the total number of CD8^+ T cells in CM-4T1 tumors compared to CQDs,
228 H-4T1, or PBS groups (Fig. 4e). Analysis of the 4T1 tumor tissues with antibodies for
229 CD8^+ , cleaved caspase-3 and Ki67 further revealed remarkable enhancement of
230 cytotoxic T cells response and apoptosis of cancer cells with significant reduction of
231 proliferation in the CM-4T1 therapy group of Balb/c mice (Fig. 4f).

232 To further reveal potentials of the CM-cancer, we introduced a transgenic mouse
233 model that carried a triple-negative mammary tumor in form of *Fgfr2-S252W*, and
234 designed a personalized therapeutic protocol. When the primary mammary tumors in
235 the *Fgfr2-S252W* mice reached at about 500–750 mm³ in size, a part of the tumors were
236 surgically taken out from the mouse body for producing CM-cancer. The mice were
237 randomized into two groups: the therapeutic group with injection of the CM-cancer
238 (*Fgfr2-S252W*), and the control group with injection of PBS only. In comparison with
239 the control group, the *Fgfr2* tumors in the therapeutic group were significantly inhibited.
240 And the anti-cancer T cell response in the primary tumor site and inhibition of the lung
241 metastasis could also be observed in the therapeutic group. Above data suggested that
242 CM-cancer possessed enormous potential on personalized immunotherapeutics.

243 4T1 tumor have strong spontaneous metastatic capability⁴¹. In the therapy group
244 with CM-4T1 in Balb/c mice with 4T1 tumor, the lung metastases of 4T1 tumors were
245 significantly inhibited in contrast with the control groups of P1-P4, as shown in Fig. 4g,
246 4h. Through comparison of the H&E staining tissue slices of the excised main organs
247 from the five groups, surprisingly we observed that all cancer metastases of the 4T1
248 carcinoma in organs, including lung, liver and spleen, were perfectly inhibited by the
249 CM-4T1 therapy, as shown in Fig. 4i. The immunotherapy efficacy of the CM-cancer
250 for metastatic cancer was further studied in a 4T1 mammary cells transplanted
251 spontaneous metastasis mouse models (Fig. 5). The 4T1 primary tumors were surgically
252 removed out at about 500–750 mm³ in size, and the mice were randomized into the
253 therapy group of (M0) with the CM-4T1, and four control groups of (M1) PBS, (M2)
254 pure CQDs, (M3) H-4T1, and (M4) CM-EMT6, respectively. In comparison with the
255 H&E staining slices of lung and liver, the number of metastatic nodules in the therapy
256 group (M0) were significantly reduced with the lowest number of macroscopic
257 metastatic nodules among the five groups (Fig. 5c). By checking the characteristic
258 protein expression levels of cytotoxic T cells (CD8⁺), MPs (F4/80), DCs (CD11c) and
259 cytokine (IFN- γ) in lung tissues, we observed that anti-cancer immune response was

260 the highest in the therapy group (M0), indicating feasibility and effectiveness of the
261 personalized CM-cancer for metastatic cancer immunotherapy (Fig. 5d).

262 In summary, we developed a unique method of composing cancer cells with
263 CQDs to prepare CM-cancer for personalized cancer immunotherapy. The
264 enhancement in immunogenicity of the CM-cancer were obvious, as evidenced by a
265 number of mice and zebrafish experiments. The CM-cancer efficiently recruited and
266 activated MPs and DCs, then effectively delivered the cancer antigens into the lymph
267 nodes to activate cytotoxic T cells, and finally led to a specific anti-cancer immune
268 response for the whole body to kill primary and metastatic tumors. More importantly,
269 the whole preparation time of the CM-cancer took only several hours, which provides
270 a distinct and incomparable advantage for customarized cancer immunotherapy. Our
271 research reported in this paper intelligently and fruitfully demonstrated a facile, low
272 cost, quick and most importantly very efficient cancer immunotherapy technology. This
273 technology would be acting as a shining light in the area of cancer immunotherapy.

274

275 **References**

- 276 1. Cahill, D. P. et al. Mutations of mitotic checkpoint genes in human cancers. *Nature*
277 **392**, 300–303(1998).
- 278 2. Hofree, M. et al. Network-based stratification of tumor mutations. *Nat. Methods*
279 **10**, 1108–1115(2013).
- 280 3. Mellman, I., Coukos, G. & Dranoff, G. Cancer immunotherapy comes of age.
281 *Nature* **480**, 480–489 (2011).
- 282 4. Sahin, U. & Türeci, Ö. Personalized vaccines for cancer immunotherapy. *Science*
283 **359**, 1355–1360 (2018).
- 284 5. Ott, P. A. et al. An immunogenic personal neoantigen vaccine for patients with
285 melanoma. *Nature* **547**, 217–221(2017).
- 286 6. Bulik–Sullivan, B. et al. Deep learning using tumor HLA peptide mass
287 spectrometry datasets improves neoantigen identification. *Nat. Biotech.* **37**, 55–
288 63(2019).

- 289 7. Khodadoust, M. S. et al. Antigen presentation profiling reveals recognition of
290 lymphoma immunoglobulin neoantigens. *Nature* **543**, 723–727(2017).
- 291 8. Sahin, U. et al. Personalized RNA mutanome vaccines mobilize poly-specific
292 therapeutic immunity against cancer. *Nature* **547**, 222–226 (2017).
- 293 9. Gong, N. et al. Proton-driven transformable nanovaccine for cancer
294 immunotherapy. *Nat. Nanotech.* **15**, 1053–1064 (2020).
- 295 10. Damo, M. et al. Inducible de novo expression of neoantigens in tumor cells and
296 mice. *Nat. Biotech.* **39**, 64–73(2021).
- 297 11. Van der Burg, S. H. et al. Vaccines for established cancer: overcoming the
298 challenges posed by immune evasion. *Nat. Rev. Cancer* **16**, 219–233 (2016).
- 299 12. Bradley, C. A. CD24—a novel ‘don’t eat me’ signal. *Nat. Rev. Cancer* **19**, 541–
300 541(2019).
- 301 13. Elward, K. & Gasque, P. “Eat me” and “don’t eat me” signals govern the innate
302 immune response and tissue repair in the CNS: emphasis on the critical role of the
303 complement system. *Mol. Immunol.* **40**, 85–94(2003).
- 304 14. Paidassi, H. et al. How phagocytes track down and respond to apoptotic cells. *Crit.*
305 *Rev. Immunol.* **29**, 111–130 (2009).
- 306 15. Czaja, A. J. Immune inhibitory proteins and their pathogenic and therapeutic
307 implications in autoimmunity and autoimmune hepatitis. *Autoimmunity* **52**, 144–
308 160 (2019).
- 309 16. Shrestha, A. C. et al. Cytolytic perforin as an adjuvant to enhance the
310 immunogenicity of DNA vaccines. *Vaccines* **7**, 38(2019).
- 311 17. Zhang, Y. N. et al. Nanoparticle size influences antigen retention and presentation
312 in lymph node follicles for humoral immunity. *Nano Lett.* **19**: 7226–7235(2019).
- 313 18. Lynn, G. M. et al. In vivo characterization of the physicochemical properties of
314 polymer-linked TLR agonists that enhance vaccine immunogenicity. *Nat. Biotech.*
315 **33**, 1201–1210(2015).
- 316 19. Pardoll, D. M. The blockade of immune checkpoints in cancer immunotherapy. *Nat.*
317 *Rev. Cancer* **12**, 252–264(2012).

- 318 20. Ribas, A. & Wolchok, J. D. Cancer immunotherapy using checkpoint blockade.
319 *Science* **359**, 1350–1355 (2018).
- 320 21. Han, X. et al. Red blood cell–derived nanoerythroosome for antigen delivery with
321 enhanced cancer immunotherapy. *Sci. Adv.* **5**, eaaw6870 (2019).
- 322 22. Patel, S. A. & Minn, A. J. Combination cancer therapy with immune checkpoint
323 blockade: Mechanisms and strategies. *Immunity* **48**, 417–433 (2018).
- 324 23. Bao, X. et al. In vivo theranostics with near–infrared–emitting carbon dots—highly
325 efficient photothermal therapy based on passive targeting after intravenous
326 administration. *Light Sci. Appl.* 1–11(2018).
- 327 24. Liu, C. et al. Nano–carrier for gene delivery and bioimaging based on carbon dots
328 with pei–passivation enhanced fluorescence. *Biomaterials* **33**, 3604–3613 (2012).
- 329 25. Li, S. et al. Targeted tumour theranostics in mice via carbon quantum dots
330 structurally mimicking large amino acids. *Nat. Biomed. Eng.* **4**, 704–716 (2020).
- 331 26. Liang, T. et al. Morphology Control of Luminescent Carbon Nanomaterials: From
332 Dots to Rolls and Belts. *ACS nano* (2020).
- 333 27. Liu, E. et al. Enhanced Near–Infrared Emission from Carbon Dots by Surface
334 Deprotonation. *J. Phys. Chem. Lett.* **12**, 604–611(2020).
- 335 28. Damodaran, S. In situ measurement of conformational changes in proteins at liquid
336 interfaces by circular dichroism spectroscopy. *Anal. Bioanal. Chem.* **376**, 182–
337 188(2003).
- 338 29. Palucka, K. & Banchereau, J. Cancer immunotherapy via dendritic cells. *Nat. Rev.*
339 *Cancer* **12**, 265–277(2012).
- 340 30. Jaynes, J. M. et al. Mannose receptor (CD206) activation in tumor–associated
341 macrophages enhances adaptive and innate antitumor immune responses. *Sci.*
342 *Transl. Med.* **12**, (2020).
- 343 31. Nizet, V. & Johnson, R. S. Interdependence of hypoxic and innate immune
344 responses. *Nat. Rev. Immunol.* **9**, 609–617(2009).
- 345 32. Shen, L. H. et al. Oxidized low–density lipoprotein induces differentiation of
346 RAW264. 7 murine macrophage cell line into dendritic–like cells. *Atherosclerosis*

- 347 **199**, 257–264(2008).
- 348 33. He, X. et al. Visualization of human T lymphocyte-mediated eradication of cancer
349 cells in vivo. *Proc. Natl. Acad. Sci. U. S. A.* **117**, 22910–22919(2020).
- 350 34. Tao, J. et al. Toward understanding the prolonged circulation and elimination
351 mechanism of Crosslinked polymeric micelles in zebrafish model. *Biomaterials*
352 **256**, 120180(2020).
- 353 35. Ellett, F. et al. *mpeg1* promoter transgenes direct macrophage-lineage expression
354 in zebrafish. *Blood* **117** E49–E56(2011).
- 355 36. Sanderson, L. E. et al. An inducible transgene reports activation of macrophages in
356 live zebrafish larvae. *Dev. Comp. Immunol.* **53**, 63-69(2015).
- 357 37. Okuda, K. S. et al. *lyve1* expression reveals novel lymphatic vessels and new
358 mechanisms for lymphatic vessel development in zebrafish. *Development* **139**,
359 2381–2391(2012).
- 360 38. Langenau, D. M. et al. In vivo tracking of T cell development, ablation, and
361 engraftment in transgenic zebrafish. *Proc. Natl. Acad. Sci. U. S. A.* 2004, **101**:
362 7369–7374(2004).
- 363 39. Luo, K. Q. et al. Application of the fluorescence resonance energy transfer method
364 for studying the dynamics of caspase-3 activation during UV-induced apoptosis in
365 living HeLa cells. *Biochem. Biophys. Res. Commun.* **283**, 1054–1060(2001).
- 366 40. Fu, A. et al. Rapid identification of antimicrometastases drugs using integrated
367 model systems with two dimensional monolayer, three dimensional spheroids, and
368 zebrafish xenotransplantation tumors. *Biotechnol. Bioeng.* **115**, 2828-2843(2018).
- 369 41. Yang, L. et al. Disease progression model of 4T1 metastatic breast cancer. *J*
370 *Pharmacokinet Pharmacodyn* 47, 105–116 (2020)
- 371 42. Blass, E. & Ott, P A. Advances in the development of personalized neoantigen-
372 based therapeutic cancer vaccines. *Nat. Rev. Clin. Oncol.* **2021**, 1–15 (2021).
- 373 43. Scheiblhofer, S., Laimer, J., Machado, Y., Weiss, R. & Thalhamer J. Influence
374 of protein fold stability on immunogenicity and its implications for vaccine
375 design. *Expert Rev Vaccines.* **16**, 479–489(2017).

- 376 44. Klein, L., Robey, E. A. & Hsieh, C. S. Central CD4⁺ T cell tolerance: deletion
377 versus regulatory T cell differentiation. *Nat. Rev. Immunol.* **19**, 7–18 (2019).
- 378 45. Wang, J. et al. Development and testing of a general amber force field. *J. Comput.*
379 *Chem.* **25**, 1157–1174(2004).
- 380 46. Jakalian, A., Jack, D. B. & Bayly, C. I. Fast, efficient generation of high-quality
381 atomic charges. AM1–BCC model: II. Parameterization and validation. *J. Comput.*
382 *Chem.* **23**, 1623–1641(2002).
- 383 47. Martínez, L. et al. PACKMOL: a package for building initial configurations for
384 molecular dynamics simulations. *J. Comput. Chem.* **30**, 2157–2164(2009).
- 385 48. Price, D. J. & Brooks, C. L. A modified TIP3P water potential for simulation with
386 Ewald summation. *J. Chem. Phys.* **121**, 10096–10103(2004).
- 387 49. Han, R. et al. Predicting physical stability of solid dispersions by machine learning
388 techniques. *J. Control. Release* **311–312**, 16–25(2009).
- 389 50. Chan, T.& Ouyang, D. Investigating the molecular dissolution process of binary
390 solid dispersions by molecular dynamics simulations. *Asian J. Pharm.* **13**, 248–
391 254(2018).
- 392 51. Luo, K. Q. et al. Application of the fluorescence resonance energy transfer method
393 for studying the dynamics of caspase–3 activation during UV–induced apoptosis
394 in living HeLa cells. *Biochem. Biophys. Res. Commun.* **283**, 1054–1060(2001).
- 395 52. Fu, A. et al. Rapid identification of antimicrometastases drugs using integrated
396 model systems with two dimensional monolayer, three dimensional spheroids, and
397 zebrafish xenotransplantation tumors. *Biotechnology and Bioengineering* **115**,
398 2828–2843(2018).
- 399 53. Deng, S. et al. Biodegradable polymeric micelle–encapsulated doxorubicin
400 suppresses tumor metastasis by killing circulating tumor cells. *Nanoscale*, **7**,
401 5270–80(2015).

402

403 **Acknowledgments**

404 The authors wish to acknowledge Prof. Ming Yuen Lee for providing *Tg(lck:EGFP)*

405 transgenic zebrafish, and the Animal Facility of the Faculty of Health Sciences,
406 University of Macau for providing the animal housing.

407

408 **Fundings**

409 National Natural Science Foundation of China 61922091. Science and Technology.
410 Development Fund (Macau) 0040/2019/A1, 0011/2019/AKP, 0015/2018/A1. Research
411 and Development Grant for Chair Professor Fund from the University of Macau
412 CPG2020-00026-IAPME, CPG2021-00034-IAPME, CPG2021-00021-FHS. Research
413 Grant from the University of Macau MYRG2019-00103-IAPME, SRG2019-00163-
414 IAPME, MYRG2017-00200-ICMS.

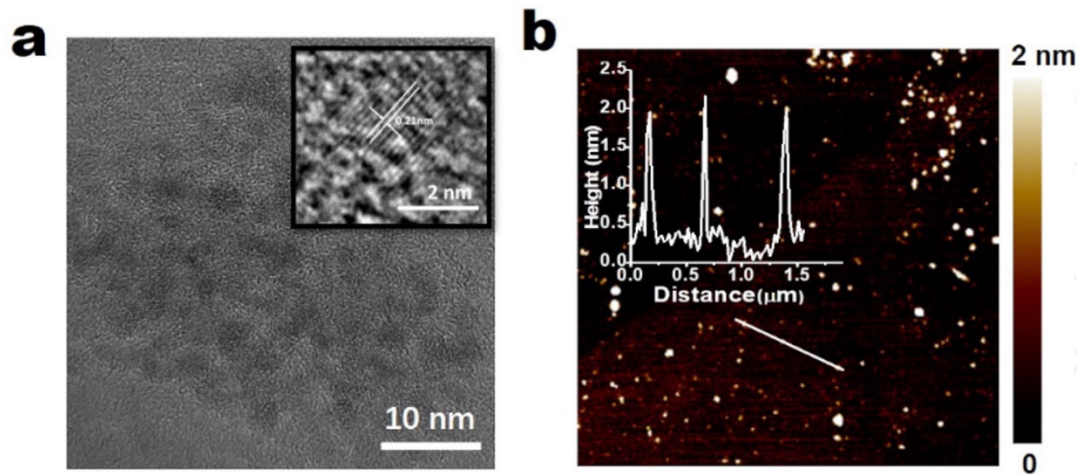
415

416 **Author contributions**

417 Z. K. Tang led and designed the whole project, and involved every steps of the
418 investigation. S. N. Qu discovered the CQD-based anti-cancer immunotherapy
419 phenomena, and participated the whole project investigations. C. X. Deng led the part
420 of biomedicine study and designed cancer immunotherapy using various mouse models.
421 T. Liang focused the CQDs synthesis and participated all investigations including the
422 biomedicine experiments. H. P. Lei focused the biomedicine and conducted experiments
423 for cancer treatment and immunotherapy using various mice models. S. Guo
424 participated experiments for cancer treatment and immunotherapy using various mouse
425 models. Y. Zheng together with J. S. Tao contributed the zebrafish experiments. W. Ge
426 offered *Tg (mpeg1:EGFP)* transgenic zebrafish model and guidance for zebrafish
427 experiments. Q. Luo provided *B16F10-C* transgenic zebrafish model. D. F. Ouyang
428 together with H. L. Gao performed the MD simulation of CQDs and BSA complexation.

429

430

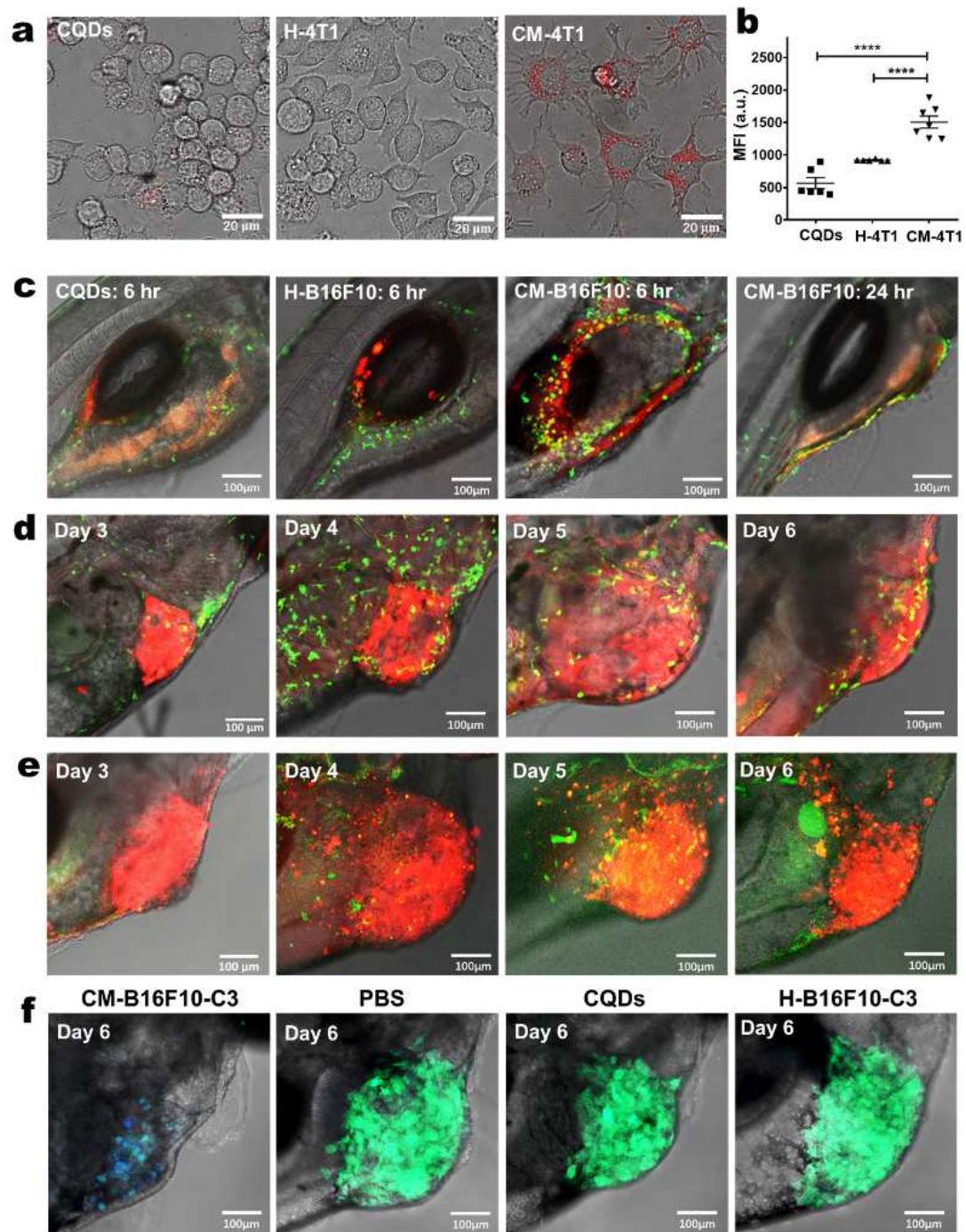


431

432 **Fig. 1. characterization of CQDs. (a)** TEM image of CQDs; inset: HRTEM image of a CQD; **(b)** AFM

433 image of CQDs; inset: height distribution of the CQDs.

434

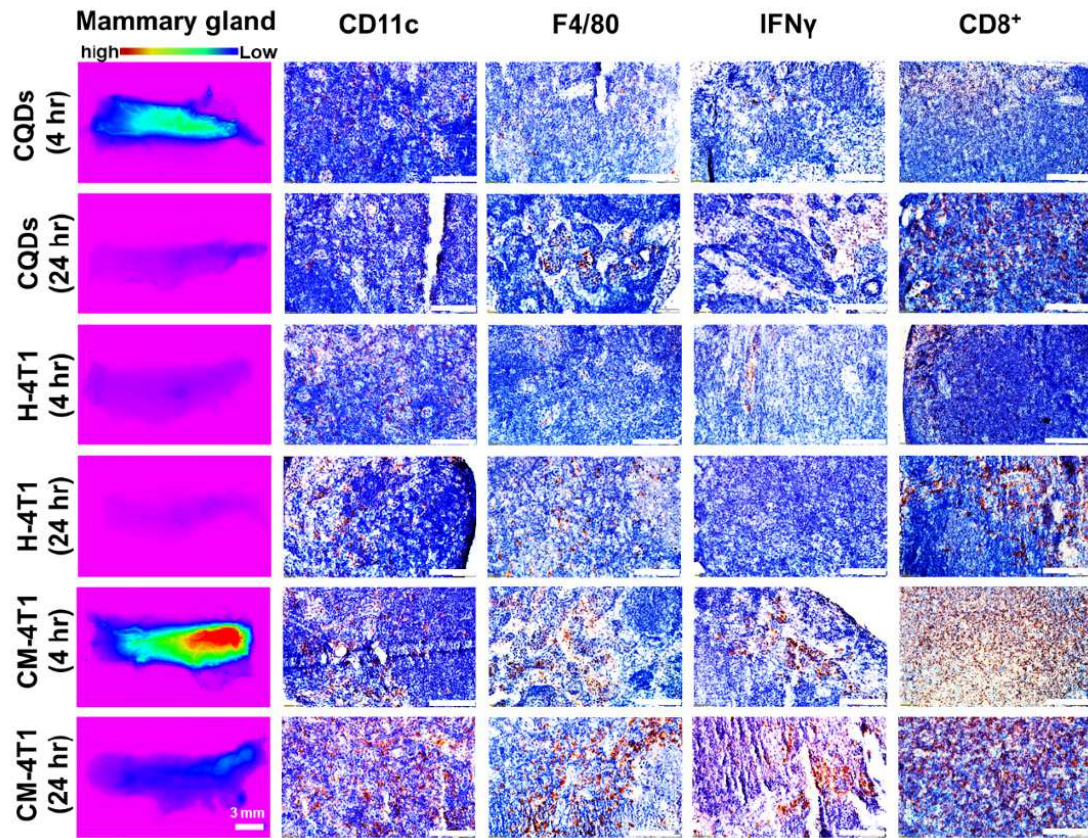


435

436 **Fig. 2. CM-cancer induced hyperactivation of MPs and anti-cancer immune response in zebrafish**
 437 **model.** (a) CLSM images of the MPs, from left to right : after co-incubating with CQDs, H-4T1 and CM-
 438 4T1, respectively; (b) MHC-II marked fluorescence intensities (MFI) from the MP cells in different
 439 treating groups; data were collected using a flow cytometer after the MPs were cultured in vitro with H-
 440 4T1 ($n = 6$), CQDs ($n = 6$) and CM-4T1 ($n = 7$), respectively, for 24 hr. $p < 0.0001$ (****). CQDs: 50
 441 $\mu\text{g/ml}$, 4T1 cells: $1 \times 10^7/\text{ml}$, respectively. Data plotted are mean \pm S.E.M; (c) From left to right, CLSM

442 images of MPs (Green) response in *Tg(mpeg1:EGFP)* transgenic zebrafish model after abdominal
443 injection with CQDs (Red), DiI dyes labeled H-B16F10 (Red) and CM-B16F10 (Red), respectively, at
444 equivalent dose at 4 nl for 6 hr and 24 hr; CQDs: 200 µg/ml, B16F10 cells: 1×10^7 /ml, 4 nl; **(d)** CLSM
445 images of the MPs response in DiI labelled B16F10 cancer xenograft *Tg(mpeg1:EGFP)* zebrafish model
446 treated with CM-B16F10; MPs (Green), B16F10 cells (Red); **(e)** CLSM images of the anti-cancer T cells
447 response in DiI labelled B16F10 cancer xenograft *Tg(lck:EGFP)* zebrafish model treated with CM-
448 B16F10, T cells (Green), B16F10 cells (Red); **(f)** CLSM images of monitoring the cancer cell
449 proliferation growth (Green) and detect the caspase-3 activation based apoptotic (Blue) by FRET imaging
450 in B16F10-C3 cancer xenograft zebrafish model after PBS, CQDs, H-B16F10-C3 and CM-B16F10-C3
451 treatments at day 6, respectively.

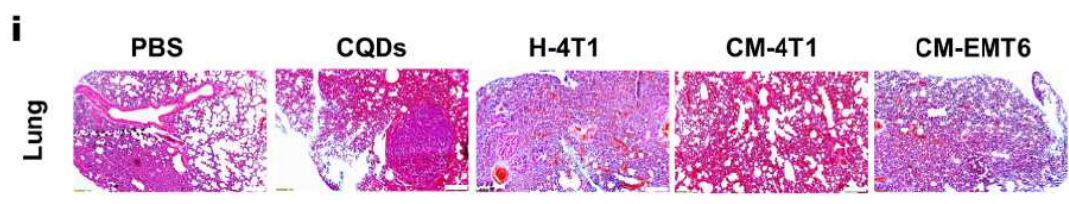
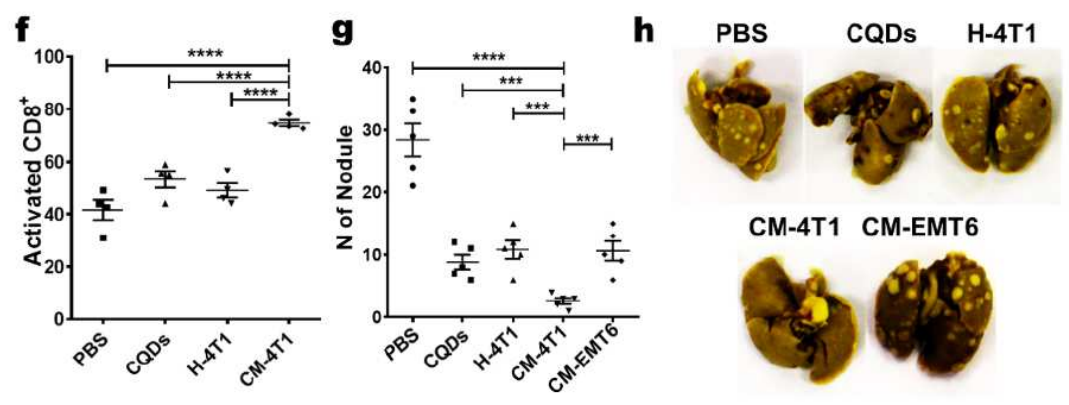
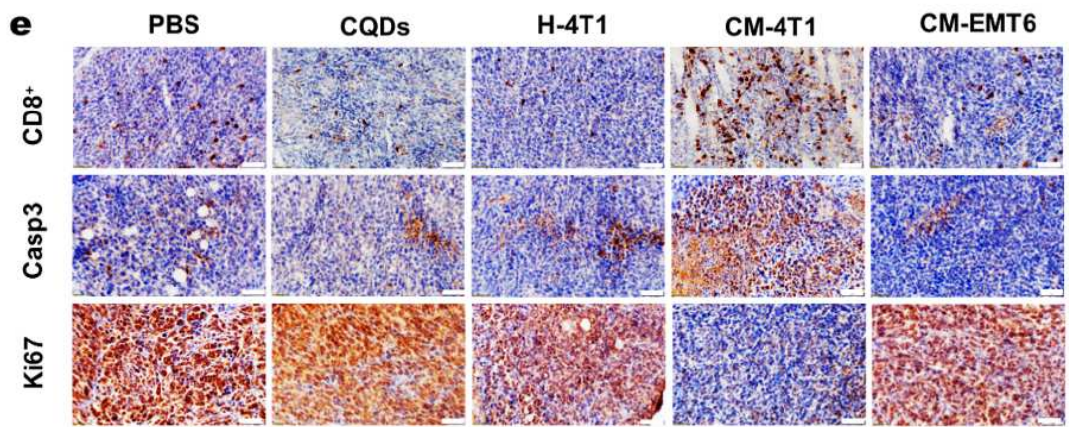
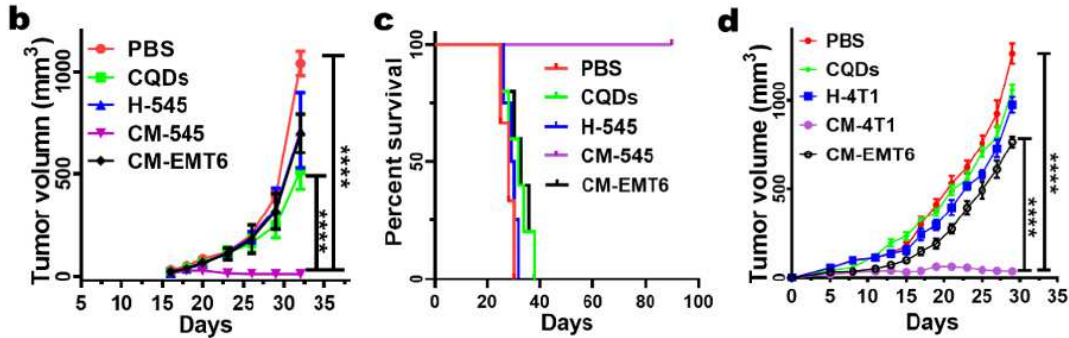
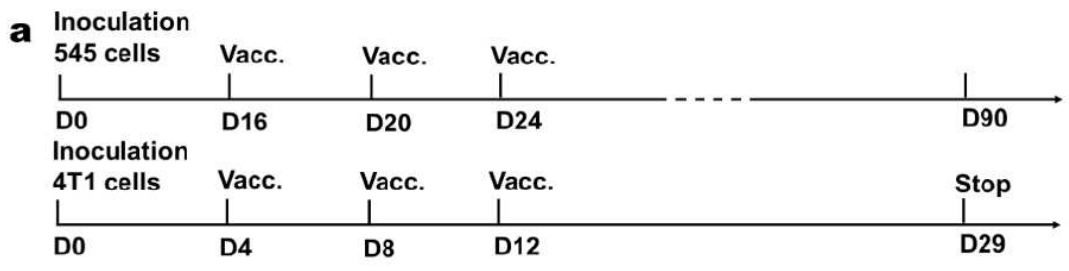
452



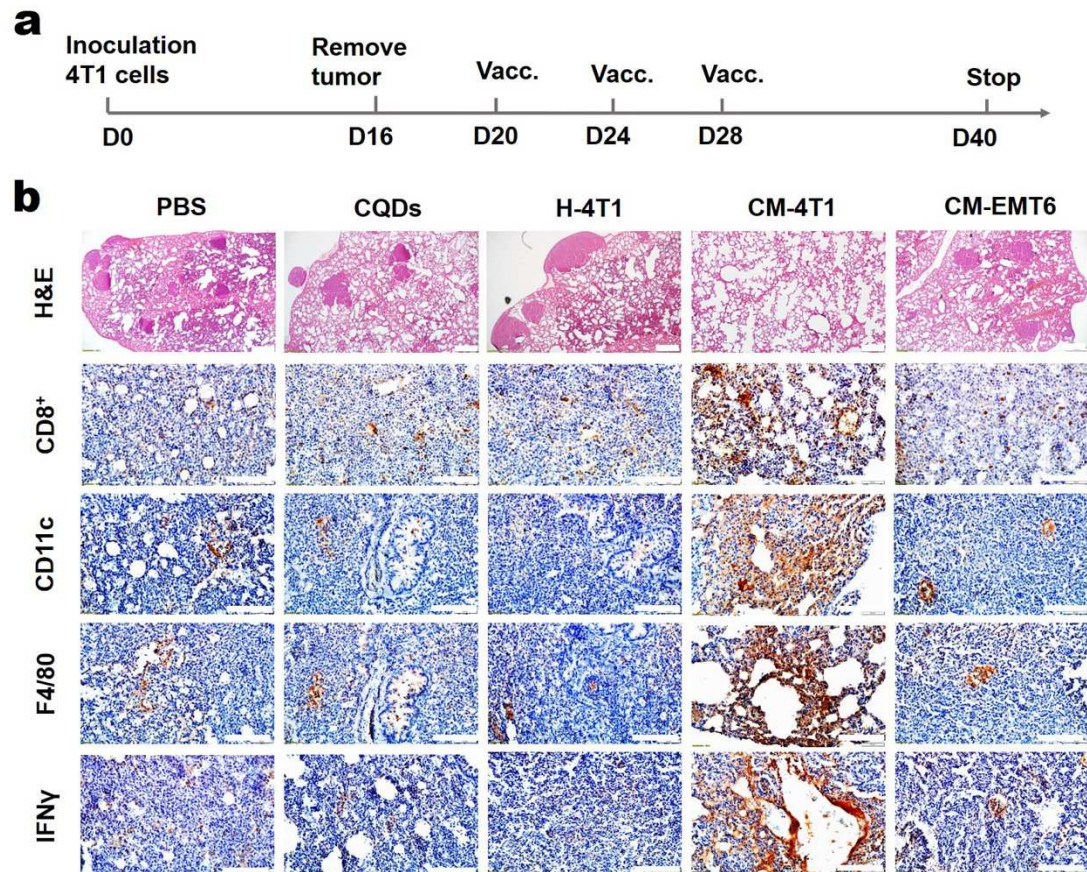
453

454 **Fig. 3. The CM-cancer generates robust immune responses in lymph node.** Fluorescent images of
 455 the 4th mammary tissue with inguinal lymph node (left) after abdominal injection with CQDs, H-4T1
 456 labeled with fluorescent dyes (DID 700) and CM-4T1, respectively, at equivalent dose (200 μ l per mice)
 457 at 4 hr and 24 hr (Scale bar: 3 mm), 647 nm excitation (BA 700 nm). IHC staining of the lymph nodes
 458 against CD11c, F4/80, IFN γ , and CD8⁺ with indicated treatment groups (Scale bar: 100 μ m).

459



461 **Fig. 4. CM-cancer inhibits tumor growth and metastasis on murine mammary cancer models. (a)**
462 Schematic illustration of CM-545 and CM-4T1 to inhibit primary 545 tumor in FVB and 4T1 tumor in
463 Balb/c murine mammary model, respectively; **(b)** Growth curves of 545 tumors and **(c)**, percent survival
464 of FVB murine treated with CM-545 ($n = 6$), CM-EMT6 ($n = 5$), H-545 ($n = 5$), PBS ($n = 5$) and CQDs
465 ($n = 5$), $p < 0.0001$ (****). Data plotted are mean \pm S.E.M.; **(d)** Growth curves of 4T1 tumors in mice
466 treated with CM-4T1 ($n = 6$), CM-EMT6 ($n = 6$), H-4T1 ($n = 6$), PBS ($n = 6$) and CQDs ($n = 6$), $p <$
467 0.0001 (****). Data plotted are mean \pm S.E.M; **(e)** IHC staining of tumor sections from orthotopic
468 transplantation model showing that the CM-4T1 treatment suppressed the expression of CD8⁺, Ki67 and
469 induced Cleaved Casp3. Scale bar: 50 μ m; **(f)** Representative flow cytometry ratios of activated CD8⁺ T
470 cells in the tumors from different groups after CM-4T1, CQDs, H-4T1 and PBS treatments ($n = 4$),
471 respectively. $p < 0.0001$ (****). Data plotted are mean \pm S.E.M; **(g)** Statistics, and **(h)** images of
472 metastatic tumors in lungs from P0-4 groups after PBS, CQDs, H-4T1, CM-EMT6 and CM-4T1
473 treatments ($n = 5$), respectively. $p < 0.0001$ (****), $p = 0.0007$ (***), $p = 0.0004$ (***), $p = 0.0008$ (***).
474 Data plotted are mean \pm S.E.M; **(i)** H&E staining of lungs from P0-4 groups of 4T1 murine mammary
475 model mice. Scale bar: 200 μ m.
476



477

478 **Fig. 5. CM-4T1 cures metastatic cancer on a postoperative 4T1 murine mammary model. (a)**

479 Schematic illustration of CM-4T1 treating the post-surgical 4T1 murine mammary model; (c) H&E and

480 IHC staining of lung tissues from M0-M4 groups after PBS, CQDs, H-4T1, CM-EMT6 and CM-4T1

481 treatments, respectively. Scale bar: 100 μ m.

Figures

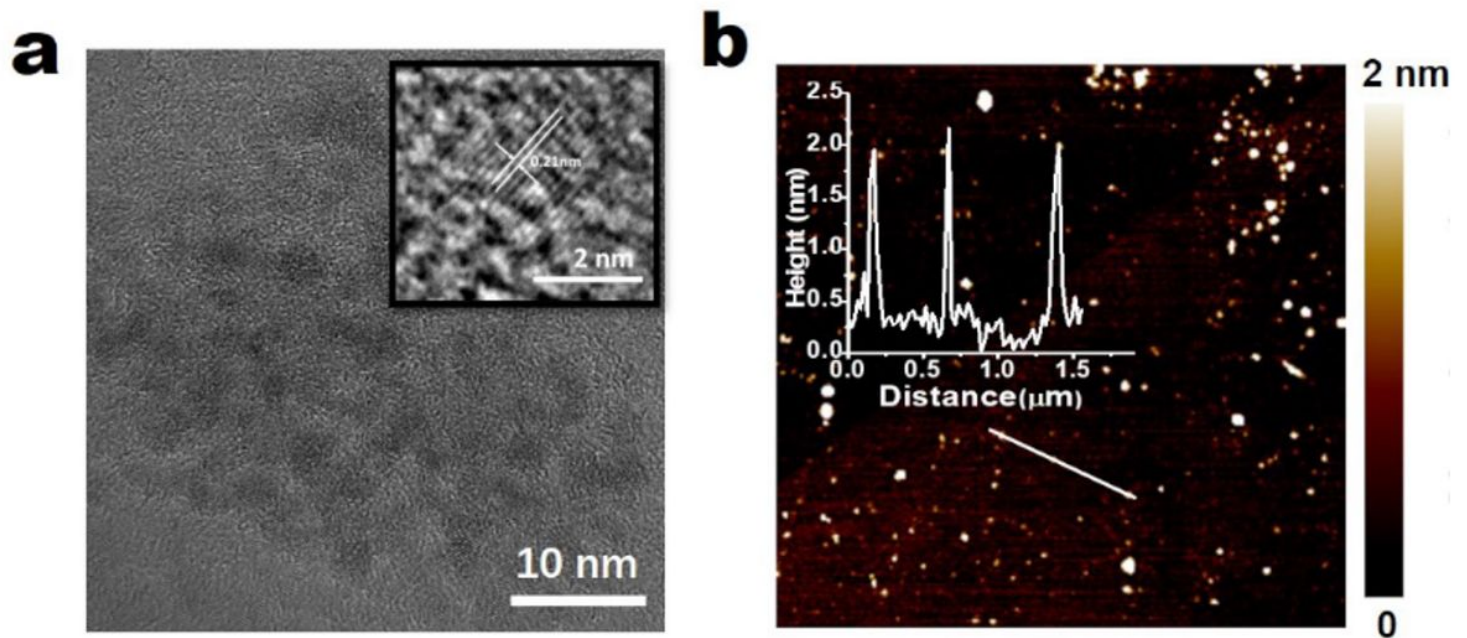


Figure 1

Characterization of CQDs. (a) TEM image of CQDs; inset: HRTEM image of a CQD; (b) AFM image of CQDs; inset: height distribution of the CQDs.

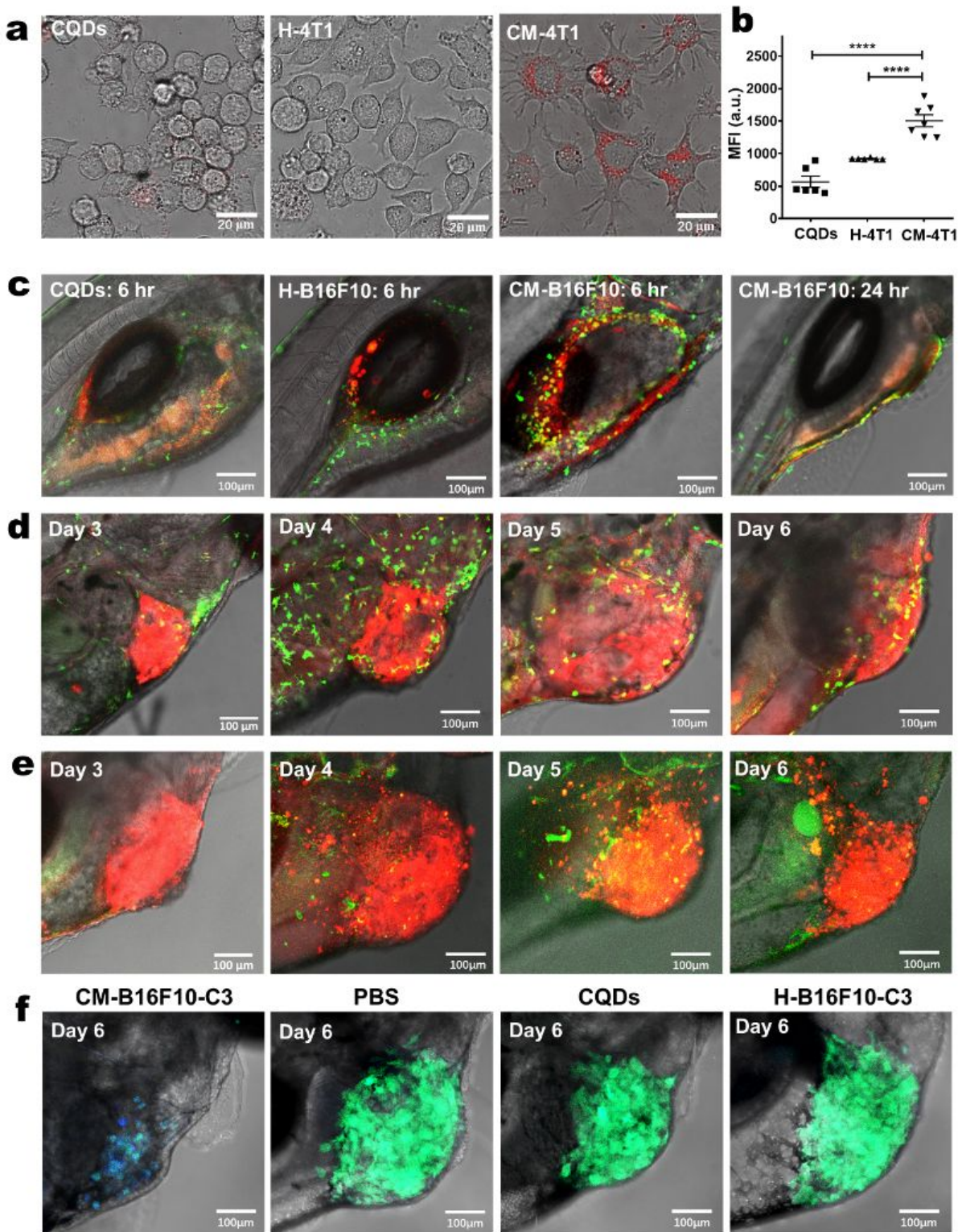


Figure 2

CM-cancer induced hyperactivation of MPs and anti-cancer immune response in zebrafish model. (a) CLSM images of the MPs, from left to right : after co-incubating with CQDs, H-4T1 and CM- 4T1, respectively; (b) MHC-II marked fluorescence intensities (MFI) from the MP cells in different treating groups; data were collected using a flow cytometer after the MPs were cultured in vitro with H- 4T1 (n = 6), CQDs (n = 6) and CM-4T1 (n = 7), respectively, for 24 hr. $p < 0.0001$ (****). CQDs: 50 $\mu\text{g}/\text{ml}$, 4T1 cells:

1×10⁷/ml, respectively. Data plotted are mean ± S.E.M; (c) From left to right, CLSM images of MPs (Green) response in Tg(mpeg1:EGFP) transgenic zebrafish model after abdominal injection with CQDs (Red), Dil dyes labeled H-B16F10 (Red) and CM-B16F10 (Red), respectively, at equivalent dose at 4 nl for 6 hr and 24 hr; CQDs: 200 µg/ml, B16F10 cells: 1×10⁷/ml, 4 nl; (d) CLSM images of the MPs response in Dil labelled B16F10 cancer xenograft Tg(mpeg1:EGFP) zebrafish model treated with CM-B16F10; MPs (Green), B16F10 cells (Red); (e) CLSM images of the anti-cancer T cells response in Dil labelled B16F10 cancer xenograft Tg(lck:EGFP) zebrafish model treated with CM448 B16F10, T cells (Green), B16F10 cells (Red); (f) CLSM images of monitoring the cancer cell proliferation growth (Green) and detect the caspase-3 activation based apoptotic (Blue) by FRET imaging in B16F10-C3 cancer xenograft zebrafish model after PBS, CQDs, H-B16F10-C3 and CM-B16F10-C3 treatments at day 6, respectively.

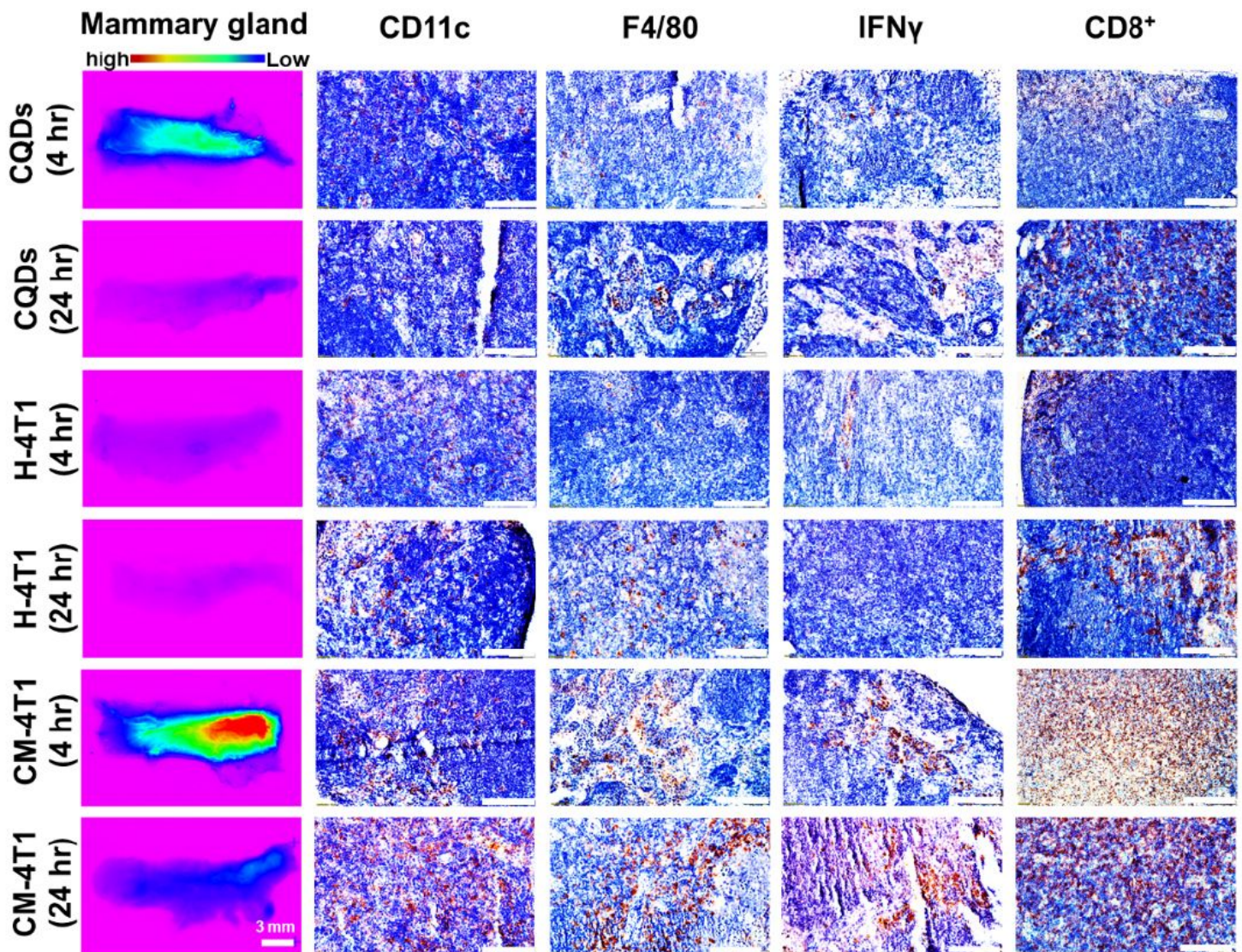


Figure 3

The CM-cancer generates robust immune responses in lymph node. Fluorescent images of the 4th mammary tissue with inguinal lymph node (left) after abdominal injection with CQDs, H-4T1 labeled with fluorescent dyes (DID 700) and CM-4T1, respectively, at equivalent dose (200 µl per mice) at 4 hr and 24

hr (Scale bar: 3 mm), 647 nm excitation (BA 700 nm). IHC staining of the lymph nodes against CD11c, F4/80, IFN γ , and CD8+ with indicated treatment groups (Scale bar: 100 μ m).

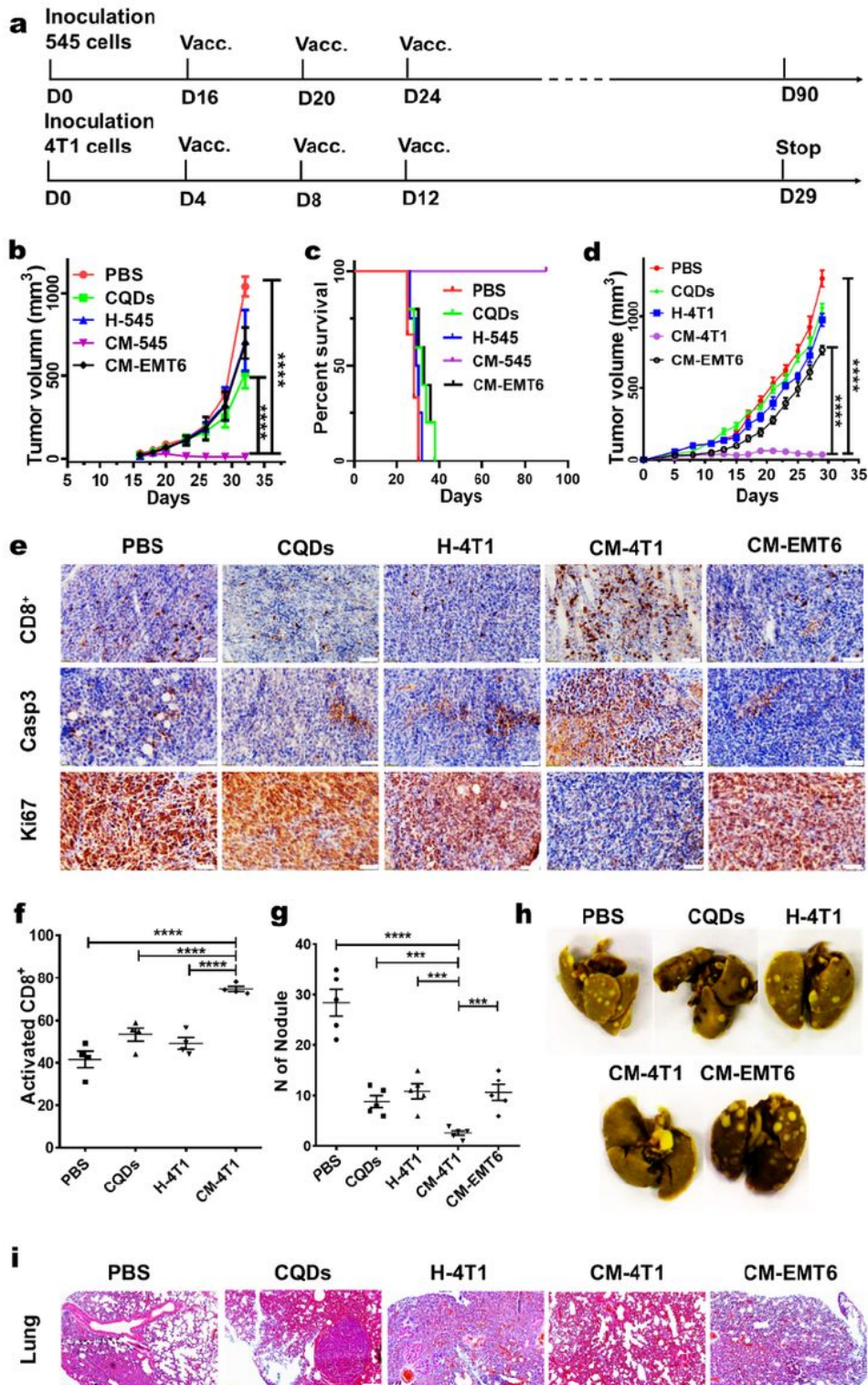


Figure 4

CM-cancer inhibits tumor growth and metastasis on murine mammary cancer models. (a) Schematic illustration of CM-545 and CM-4T1 to inhibit primary 545 tumor in FVB and 4T1 tumor in Balb/c murine mammary model, respectively; (b) Growth curves of 545 tumors and (c), percent survival of FVB murine

treated with CM-545 (n = 6), CM-EMT6 (n = 5), H-545 (n = 5), PBS (n = 5) and CQDs (n = 5), $p < 0.0001$ (****). Data plotted are mean \pm S.E.M.; (d) Growth curves of 4T1 tumors in mice treated with CM-4T1 (n = 6), CM-EMT6 (n = 6), H-4T1 (n = 6), PBS (n = 6) and CQDs (n = 6), $p < 0.0001$ (****). Data plotted are mean \pm S.E.M; (e) IHC staining of tumor sections from orthotopic transplantation model showing that the CM-4T1 treatment suppressed the expression of CD8+, Ki67 and induced Cleaved Casp3. Scale bar: 50 μ m; (f) Representative flow cytometry ratios of activated CD8+ T cells in the tumors from different groups after CM-4T1, CQDs, H-4T1 and PBS treatments (n = 4), respectively. $p < 0.0001$ (****). Data plotted are mean \pm S.E.M; (g) Statistics, and (h) images of metastatic tumors in lungs from P0-4 groups after PBS, CQDs, H-4T1, CM-EMT6 and CM-4T1 treatments (n = 5), respectively. $p < 0.0001$ (****), $p = 0.0007$ (***) , $p = 0.0004$ (***) , $p = 0.0008$ (***) . Data plotted are mean \pm S.E.M; (i) H&E staining of lungs from P0-4 groups of 4T1

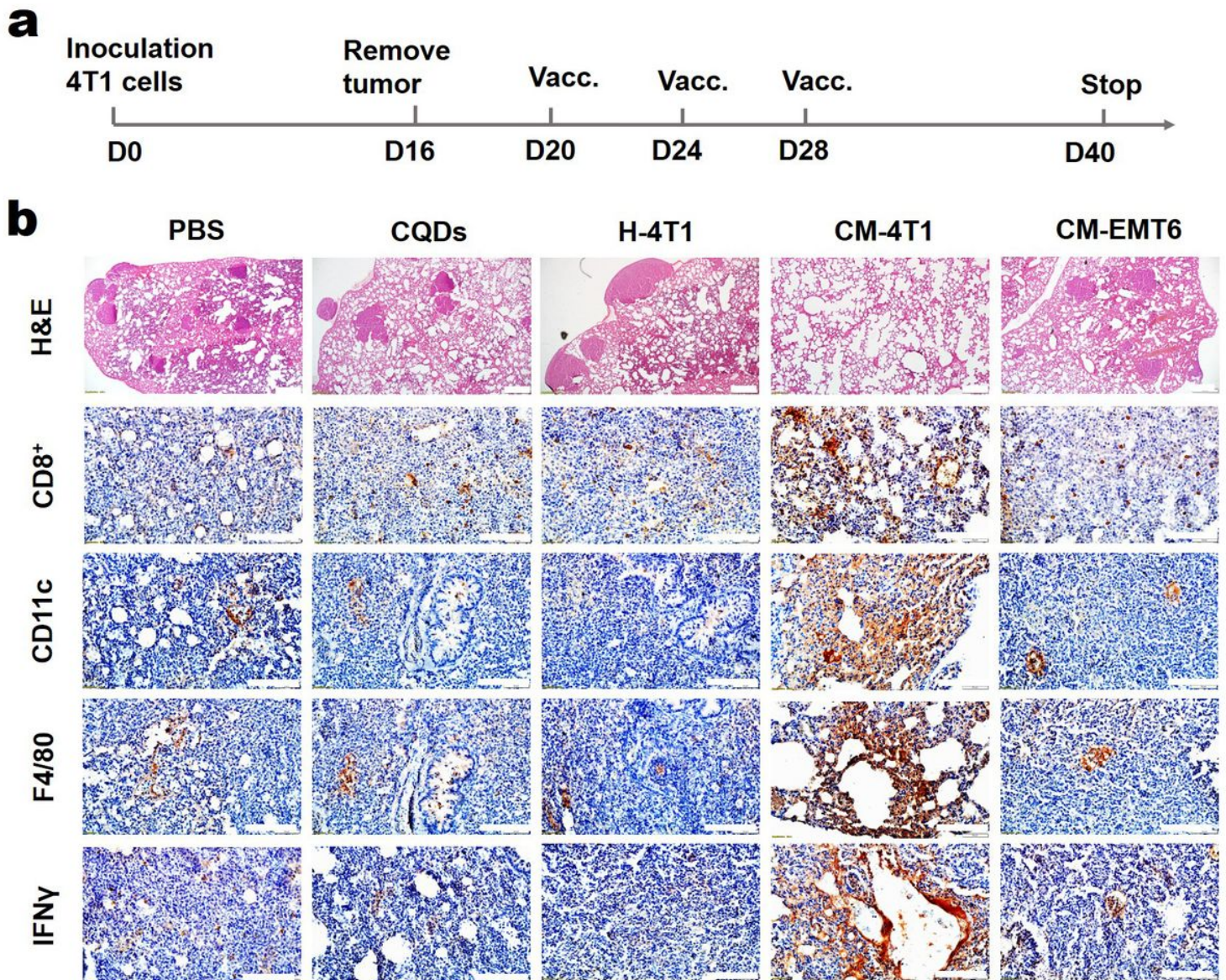


Figure 5

CM-4T1 cures metastatic cancer on a postoperative 4T1 murine mammary model. (a) Schematic illustration of CM-4T1 treating the post-surgical 4T1 murine mammary model; (c) H&E and IHC staining of lung tissues from M0-M4 groups after PBS, CQDs, H-4T1, CM-EMT6 and CM-4T1 treatments, respectively. Scale bar: 100 μm .